Solar Phys
DOI 10.1007/s11207-008-9186-8

MHD Modeling of Coronal Large-Amplitude Waves Related to CME Lift-off

J. Pomoell · R. Vainio · R. Kissmann

Received: 30 November 2007 / Accepted: 3 April 2008

Abstract We have employed a two-dimensional magnetohydrodynamic simulation code to study mass motions and large-amplitude coronal waves related to the lift-off of a coronal mass ejection (CME). The eruption of the filament is achieved by an artificial force acting on the plasma inside the flux rope. By varying the magnitude of this force, the reaction of the ambient corona to CMEs with different acceleration profiles can be studied. Our model of the ambient corona is gravitationally stratified with a quadrupolar magnetic field, resulting in an ambient Alfvén speed that increases as a function of height, as typically deduced for the low corona. The results of the simulations show that the erupting flux rope is surrounded by a shock front, which is strongest near the leading edge of the erupting mass, but also shows compression near the solar surface. For rapidly accelerating filaments, the shock front forms already in the low corona. Although the speed of the driver is less than the Alfvén speed near the top of the atmosphere, the shock survives in this region as well, but as a freely propagating wave. The leading edge of the shock becomes strong early enough to drive a metric type II burst in the corona. The speed of the weaker part of the shock front near the surface is lower, corresponding to the magnetosonic speed there. We analyze the (line-of-sight) emission measure of the corona during the simulation and recognize a wave receding from the eruption site, which strongly resembles EIT waves in the low corona. Behind the EIT wave, we clearly recognize a coronal dimming, also observed during CME lift-off. We point out that the morphology of the hot downstream region of the shock would be that of a hot erupting loop, so care has to be taken not to misinterpret

Radio Physics and the Flare-CME Relationship
Guest Editors: Karl-Ludwig Klein and Silja Pohjolainen.

J. Pomoell (✉) · R. Vainio
Department of Physics, University of Helsinki, Helsinki, Finland
e-mail: jens.pomoell@helsinki.fi

R. Vainio
e-mail: rami.vainio@helsinki.fi

R. Kissmann
Institut für Astronomie und Astrophysik, Universität Tübingen, Tübingen, Germany
e-mail: ralf.kissmann@uni-tuebingen.de

soft X-ray imaging observations in this respect. Finally, the geometry of the magnetic field around the erupting mass is analyzed in terms of precipitation of particles accelerated in the eruption complex. Field lines connected to the shock are further away from the photospheric neutral line below the filament than the field lines connected to the current sheet below the flux rope. Thus, if the DC fields in the current sheet accelerate predominantly electrons and the shock accelerates ions, the geometry is consistent with recent observations of gamma rays being emitted further out from the neutral line than hard X-rays.

Keywords Coronal mass ejections: Initiation and propagation · Energetic particles: Acceleration · Flares: Waves · Radio bursts: Type II · Waves: Shock

1. Introduction

Different kinds of large-amplitude waves in the solar corona are common during the lift-off of coronal mass ejections: metric type II radio bursts (Wild and McCready, 1950), Moreton waves (Moreton and Ramsey, 1960), and EIT waves (Thompson *et al.*, 1999) are all signatures of large-amplitude perturbations propagating at speeds from a few hundred to a couple of thousand kilometers per second (*i.e.*, at magneto-acoustic Mach numbers from slightly above unity to a few). These waves can, therefore, be regarded as signatures of fast-mode shock waves propagating through the corona.

Metric type II radio bursts, Moreton waves, and EIT waves are related to solar flares and coronal mass ejections (CMEs). In fact, in a unified view of solar eruptions, all these observational phenomena can be seen as different manifestations of a single solar eruption. There are, however, still several different interpretations about how the three different coronal disturbances are related to the eruption. Still under debate, especially, is the nature of the type II radio bursts (whether they are flare-generated blast waves or driven by mass motions related to CMEs) and EIT waves (whether they are signatures of coronal shocks, like the chromospheric Moreton waves, or smooth large-amplitude magnetosonic waves).

The roles of CMEs and flares are also a matter of debate in the genesis of yet another class of solar eruptive phenomena, that is, solar energetic particle (SEP) events. Although the impulsive SEP events – having durations from hours to a day, being electron rich and enhanced in ^{3}He and heavy ions, and showing high charge states of the heavy elements – are commonly accepted as being accelerated in impulsive flares, the acceleration processes responsible for the gradual SEP events – having durations from days to a week, being electron poor, and having "coronal" ion abundances and charge states up to MeV per nucleon energies – have been recently debated. The acceleration of these particles is usually attributed to shock waves driven by fast CMEs (Reames, 1999), and many models applying the theory of diffusive shock acceleration in shock waves propagating in the low corona have been constructed to explain particle acceleration in these events (*e.g.*, Vainio, Kocharov, and Laitinen, 2000; Vainio and Khan, 2004; Kocharov *et al.*, 2005; Sandroos and Vainio, 2007). The latest generation of spacecraft measurements, however, has revealed that, at energies above a few MeV per nucleon, many gradual events show ion abundances and charge states typical of impulsive events. Two plausible explanations have been proposed to explain these compositional signatures: *i*) a direct component from the concomitant flare (Cane *et al.*, 2006) and *ii*) reacceleration at quasi-perpendicular coronal shocks of suprathermal impulsive-flare material remnant from the impulsive flares that occurred before the CME-associated shock traversed the corona (Tylka *et al.*, 2005; Tylka and Lee, 2006; Sandroos and Vainio, 2007). Thus, the nature of shocks in the low corona is one of the key issues of particle acceleration at the Sun.

In this paper, we employ magnetohydrodynamic (MHD) simulations of CME lift-off to study the mass motions, shocks, and other large-amplitude waves induced by the CME lift-off. We pay special attention to the first few minutes of the eruption. The structure of the paper is as follows: In Section 2 we describe the MHD model, in Section 3 we present the results, in Section 4 we discuss the results, and in Section 5 we give the main conclusions of the work.

2. The Model

To study the dynamics related to CME lift-off, we solve the ideal MHD equations augmented with gravity as a source term:

$$\partial_t \rho + \nabla \cdot (\rho \mathbf{v}) = 0, \tag{1}$$

$$\partial_t (\rho \mathbf{v}) + \nabla \cdot \left(\rho \mathbf{v}\mathbf{v} + \left(P + \frac{\mathbf{B}^2}{2\mu_0} \right) I - \frac{1}{\mu_0} \mathbf{B}\mathbf{B} \right) = \rho(\mathbf{g} + \mathbf{f}), \tag{2}$$

$$\partial_t \mathcal{E} + \nabla \cdot \left[\left(\mathcal{E} + P - \frac{\mathbf{B}^2}{2\mu_0} \right) \mathbf{v} + \frac{1}{\mu_0} \mathbf{B} \times (\mathbf{v} \times \mathbf{B}) \right] = \rho \mathbf{v} \cdot (\mathbf{g} + \mathbf{f}), \tag{3}$$

$$\partial_t \mathbf{B} + \nabla \times \mathbf{E} = 0, \tag{4}$$

$$\nabla \cdot \mathbf{B} = 0, \tag{5}$$

where ρ is the mass density, $\mathbf{v}$ is the velocity, P is the gas pressure, $\mathbf{B}$ is the magnetic induction, $\mathbf{E}$ is the electric field, $\mathcal{E} = \frac{P}{\gamma - 1} + \frac{1}{2}\rho \mathbf{v}^2 + \frac{1}{2\mu_0}\mathbf{B}^2$ is the total energy density, $\mathbf{g}$ is the gravitational acceleration, and $\mathbf{f}$ is the acceleration from an additional external force field. In addition, the ideal Ohm's law $\mathbf{E} + \mathbf{v} \times \mathbf{B} = 0$ has been used. The numerical method used to solve the equations is a second-order central-upwind conservative scheme. The main idea of the method is to combine two recent developments in numerical MHD: The subsystem (1) – (3) is solved using a semi-discrete central scheme that incorporates information about the local wave propagation speeds to maintain high accuracy and achieve an upwind nature without using a Riemann solver, whereas the induction equation (4) is treated with the constrained transport technique so that Equation (5) is satisfied up to machine precision. For the details of the entire numerical scheme used in this work, we refer the reader to Ziegler (2004) and Kissmann (2007).

Since we are interested in studying the first few minutes of the solar eruption, we make a number of assumptions that significantly simplify the model. First, we take the solar surface to be flat, since the eruption evolves in a relatively small region of the corona. Second, we assume translational invariance in one of the dimensions parallel to the solar surface. Thus, the model is spatially reduced to a two-dimensional Cartesian (x, y) domain, with x chosen as the horizontal coordinate and y as the vertical coordinate increasing upward.

The spatial variation of the Alfvén speed is of great importance in determining the evolution of shocks. In most semi-empirical models (*e.g.*, Vainio and Khan, 2004), the quiet-Sun Alfvén speed increases as a function of height in the low corona. To capture this behavior in our model, we choose the gravitational acceleration to be constant, $\mathbf{g} = -g_\odot \hat{\mathbf{y}}$, and assume a constant plasma temperature for the static initial state, $T(x, y) = T_0$. With a force-free magnetic field configuration and an ideal gas law – $P = (\rho/m) k_\mathrm{B} T_0$, where $m = 0.6\, m_\mathrm{p}$ is the mean molecular mass, m_p the proton mass, and k_B Boltzmann's constant – the plasma density must then decrease exponentially for the corona to be in static

equilibrium, $\rho(x, y) = \rho_0 \mathrm{e}^{-y/H}$, where H, the scale height, is given by $H = k_\mathrm{B} T_0 / m g_\odot$. We, thus, exclude any solar wind from our model.

The magnetic field configuration consists of a detached flux rope and a quadrupolar background field. Similar to what is done in Chen *et al.* (2002), the field of the detached flux rope is created by a line current of radius r_0 situated a distance h above the solar surface, with its image current below the surface. The quadrupolar background field is created by four line currents below the surface, at positions $(\pm x_1, -d)$ and $(\pm x_2, -d)$, where d is the depth of the current lines below the solar surface. The magnetic field is thus given by the flux function $\psi = \psi_\mathrm{l} + \psi_\mathrm{i} + \psi_\mathrm{b}$ as $\mathbf{B} = B_0 \nabla \times (\psi\, \hat{\mathbf{z}})$ with the contributions from the line current ψ_l, image current ψ_i, and quadrupolar background field ψ_b given by

$$\psi_\mathrm{l} = \begin{cases} r^2/2r_0, & r \le r_0, \\ r_0/2 - r_0 \ln(r_0/r), & r > r_0, \end{cases} \tag{6}$$

$$\psi_\mathrm{i} = -\frac{r_0}{2} \ln\left[\left(x^2 + (y+h)^2\right)/l^2\right], \tag{7}$$

$$\psi_\mathrm{b} = b \ln \frac{[(x+x_1)^2 + (y+d)^2][(x-x_1)^2 + (y+d)^2]}{[(x+x_2)^2 + (y+d)^2][(x-x_2)^2 + (y+d)^2]}, \tag{8}$$

where $r = \sqrt{x^2 + (y-h)^2}$ is the distance to the center of the flux rope. Additionally, the density inside the flux rope is enhanced according to

$$\rho(x, y) = \rho_0 \left(1 + c\left(1 - \frac{r^2}{r_0^2}\right)\right), \quad r < r_0, \tag{9}$$

to model a denser filament material.

The mechanisms involved in the initiation of CMEs are still an open question. In this work, we are interested in studying perturbations produced by CMEs with different height–time profiles. A physically self-consistent initiation mechanism for such needs is beyond the scope of the current work. Instead, we apply an artificial force, $\mathbf{f} = a\, \mathrm{sgn}(v_\mathrm{f} - v)\, \hat{\mathbf{y}}$, that acts on the flux rope to drive the eruption. Here, a is the desired acceleration of the flux rope, v is the velocity of the flux rope, v_f is a desired final velocity for the flux rope, and sgn() is the sign function. Initially, the artificial force acts on the plasma elements for which $r \le r_0$. The paths of these flux rope plasma elements are then traced during the simulation to determine which elements are to be accelerated by the artificial force.

For the model parameters we choose typical coronal values: gravitational acceleration $g_\odot = 274\ \mathrm{m\,s^{-2}}$, density of the coronal base, $\rho_0 = 1.67 \times 10^{-12}\ \mathrm{kg\,m^{-3}}$, length scale $l = 2 \times 10^4$ km, and temperature $T_0 = 0.636 \times 10^6$ K, giving a scale height of $H \approx 32 \times 10^3$ km. The reason for the fine-tuning and the somewhat low value of the temperature is to produce an Alfvén speed profile that increases with height to a reasonable value at the top of the simulation box. Additionally, we adopt the values $b = 0.25$, $c = 6.25$, $x_1 = 0.3l$, $x_2 = 1.5l$, $d = 0.3l$, $B_0 = 3.38 \times 10^{-4}$ T, $h = 2.0l$, and $r_0 = 0.5l$. The parameter c is chosen so that an approximate magnetohydrostatic equilibrium is maintained inside the flux rope. Figure 1 shows the initial distribution of the density and Alfvén speed with some field lines of the magnetic field superimposed.

The grid of the simulation is a uniform Cartesian grid with 300×300 cells in the $[-10.15l, 10.15l] \times [0.15l, 20.15l]$ simulation domain. The boundary values are kept fixed during the simulation. For the bottom boundary this choice mimics a line-tying condition. For the other boundaries, the fixed boundary condition does not allow for physically correct outflow of any large-scale structure such as a CME. We thus abort the simulation when any such structure reaches one of these boundaries.

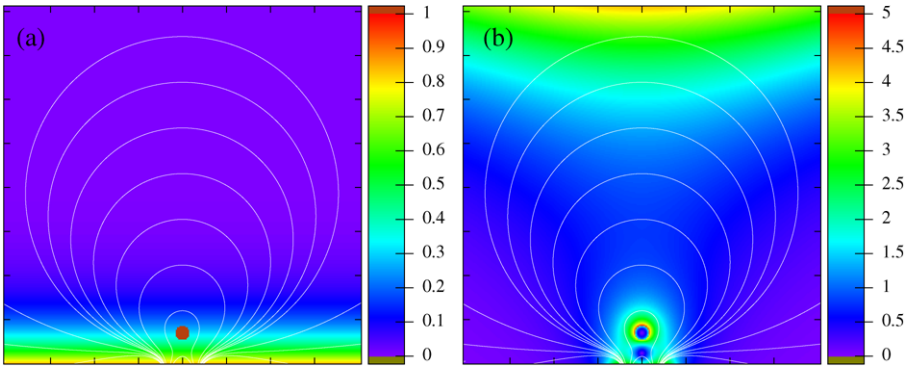

Figure 1 The initial state of the simulation, showing (a) density and (b) Alfvén speed. The white lines depict magnetic field lines. The tick marks are drawn at intervals of 5×10^4 km. The units in the color bars are for the density 1.67×10^{-12} kg m^{-3} and for the Alfvén speed 91 km s^{-1}. Note the clipping of the color bar; a brown (dark green) color indicates values larger (smaller) than the color bar maximum (minimum).

3. Results

3.1. The General Morphology of the CME Liftoff

In this section, we describe the observed phenomena in the corona as the CME lifts off. Figure 2 shows the mass density ρ (panels (a – c)), speed (panels (d – f)), compression ratio r_c, defined as $r_c = \rho(t)/(\rho_0 e^{-y/H})$ (panels (g – i)), and temperature (panels (j – l)) at three different times, $t = 330$, 550, and 770 s. The general dynamics of the eruption is as follows:

1. The flux rope starts to rise under the influence of the artificial force.
2. A perturbation surrounding the flux rope is quickly formed owing to the high Alfvén speed around the flux rope.
3. As the flux rope rises, magnetic field lines become stretched and a current sheet is formed under the flux rope. Owing to the low numerical resistivity of the scheme, no fast reconnection with fast outflow occurs in the current sheet. However, the temperature in the current sheet does rise (panels (j – l)) as a sign of reconnection. The temperature of the structures, however, remains significantly below that of the shock at the leading edge.
4. As the driving flux rope picks up speed, the outward propagating wave surrounding the flux rope develops into a shock ahead of the flux rope. The speed and strength of the shock are highest at the leading edge and decrease toward the flanks, degenerating to a fast-mode wave close to the solar surface. The speed of the wave near the surface remains roughly constant and the skirt of the wave propagates horizontally, sweeping the solar surface. Note that the shock is quasi-perpendicular both at the leading edge and at the flanks.
5. Another wave that sweeps the solar surface behind the skirt of the piston-driven shock is formed at roughly $t = 350$ s (see Figure 4).
6. Once the shock is formed, its speed exceeds that of the driving flux rope, and the shock escapes from the flux rope as its speed continues to increase owing to the increasing Alfvén speed of the ambient corona. In this sense, the shock expands more like a freely propagating wave than a driven one.
7. At the end of the simulation, when the shock approaches the upper boundary, the eruption has evolved into a large global structure. The driving flux rope has remained roughly the

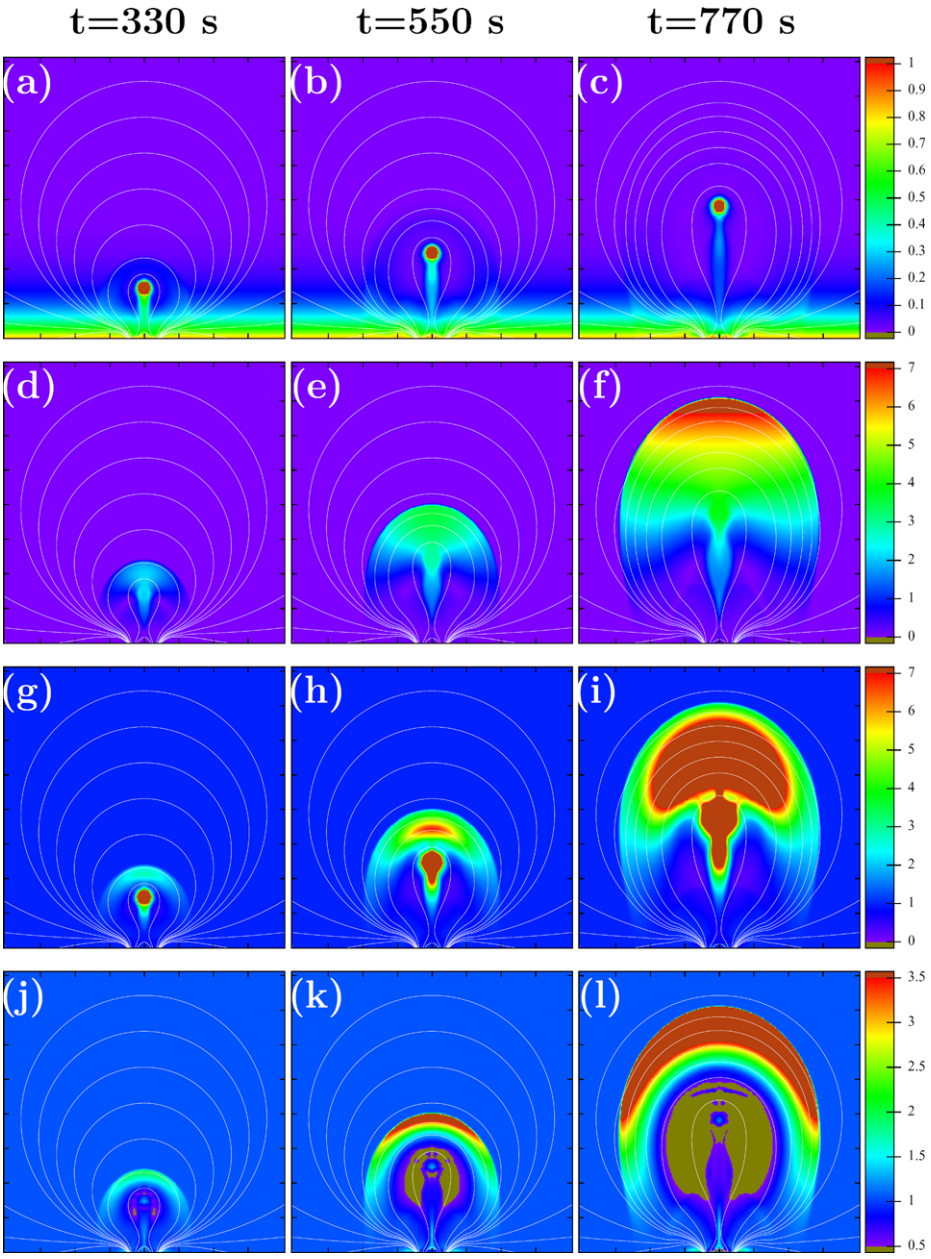

Figure 2 The density (panels (a – c)), speed (panels (d – f)), compression ratio (panels (g – i)), and temperature (panels (j – l)) at three different times, $t = 330$, 550, and 770 s. The white lines depict the magnetic field lines. The tick marks are drawn at intervals of 5×10^4 km. The units in the color bars are for the density 1.67×10^{-12} kg m^{-3}, the speed 91 km s^{-1}, and for temperature 0.636×10^6 K.

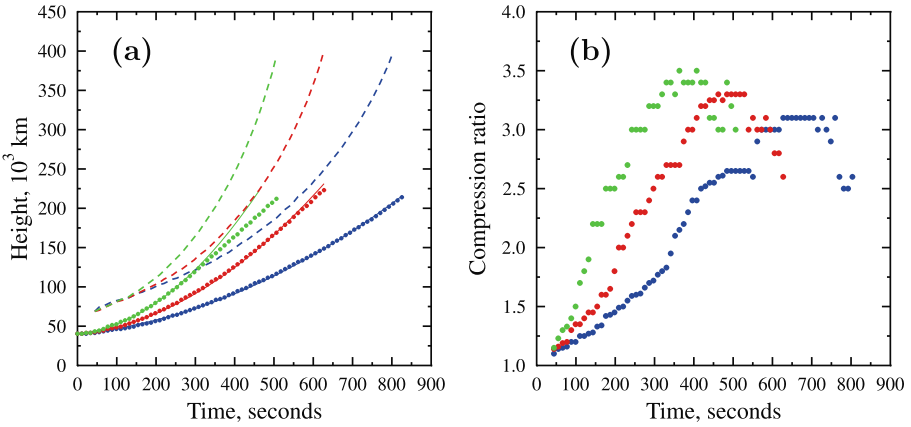

Figure 3 (a) Plot of the height – time data of the flux rope (filled circles) and shock front (broken line) for the three simulation runs. Blue corresponds to run A, red to run B, and green to run C. The solid lines are fits to the data. (b) Compression ratio of the leading edge shock as a function of time for the three runs. The color coding is the same as in panel (a).

same size during the eruption. Note also the looplike shape of the hot expanding plasma behind the shock wave.

3.2. The Effect of the Acceleration of the CME on the Coronal Waves Induced

To investigate the effect of the magnitude of the acceleration of the flux rope on the waves that are created in the corona by the eruption, we performed simulations with varying magnitudes of the artificial driving force. The height versus time plots for three runs are shown in Figure 3(a). The blue filled circles indicate the position of the flux rope for the simulation run described in the previous section (henceforth denoted run A), and the solid blue line shows a second-order fit to the data. In the same manner the red and green circles (solid lines) indicate the data (fits to the data) for runs B and C, respectively. In these runs we used a higher acceleration, as can be seen from Table 1, where we summarize the simulation parameters used and the obtained fits. Notice that for runs B and C, the flux rope quickly reaches its final constant velocity of $v_{\rm f} = 455$ km s^{-1}. The second-order polynomial has therefore been fitted to the acceleration phase only. Additionally, the time when the flux rope reaches the speed $v_{\rm f}$ and the time at which the computation is terminated are given for each simulation run in Table 1.

Table 1 The parameters a and $v_{\rm f}$ used in the artificial force and coefficients of the polynomial $h(t) = \frac{1}{2}a_{\rm fr}t^2 + v_{\rm fr}t + h_{\rm fr}$ used to fit the height–time data of the flux rope as well as the time $t_{v_{\rm f}}$ when the flux rope reaches the speed $v_{\rm f}$ and the time $t_{\rm f}$ when the computation is terminated.

	a (m s^{-2})	$v_{\rm f}$ (km s^{-1})	$a_{\rm fr}$ (m s^{-2})	$v_{\rm fr}$ (km s^{-1})	$h_{\rm fr}$ (10^3 km)	$t_{v_{\rm f}}$ (s)	$t_{\rm f}$ (s)
Run A	1030	455	400	47	40.4	–	850
Run B	1650	455	820	47	40.4	520	640
Run C	2476	455	1500	47	40.4	290	520

Additionally, in Figure 3(a), the position of the shock at the leading edge is plotted as a broken line, again with the colors indicating the corresponding simulation run. The escape of the shock from the driving flux rope can readily be seen in all three runs. Also, the first signs of the shock are seen at roughly the same height for all three runs. In Figure 3(b), the evolution of the compression ratio of the shock at the leading edge is plotted. The large scatter of the points in the figure reflects the difficulty of accurately determining the compression ratio of the shock, as there is a large density gradient also in the downstream region of the shock wave. However, the overall trend is visible. For a larger acceleration, the shock strengthens faster and has a higher peak compression ratio. The weakening of the shock as it escapes the driving flux rope into the region of high Alfvén speed is also clearly seen in all three runs.

Although the overall response of the corona to the erupting flux rope is similar for all runs (see Section 3.1), the second wave sweeping the corona behind the skirt of the shock becomes more prominent with increasing acceleration. This behavior can be seen in Figure 4, which shows the evolution of the emission measure per square arcsecond at the solar surface, calculated as $\mathrm{EM}(x) = \Delta y\, \delta^2 \sum_i n_\mathrm{e}^2(x, y_i)$, for the three runs. Here, $n_\mathrm{e} = \rho/(1.92\,m)$ is the electron density and $\delta = 725.3$ km, corresponding to a pixel size of 1 arcsecond at 1 AU. The temporal separation between the individual curves in the plots is 11 s. The emission measure shows two propagating wavelike structures. The first structure, associated with the skirt of the shock, provides a higher value of the emission measure than the ambient, which can thus be interpreted as a brightening. Behind the wave, the emission measure drops, giving rise to a dimming region. The dimming is more prominent with increasing acceleration. The emission measure of the second structure shows similar characteristics. However, the dimming region behind the second structure remains stationary once it has formed.

In Figure 5, the distance along the x-axis from $x = 0$ to the shock or large-amplitude wave front at three different heights for the three simulation runs is plotted. The shown data are for a height of $y = 20 \times 10^3$ km (solid lines), $y = 140 \times 10^3$ km (dotted lines), and $y = 260 \times 10^3$ km (broken lines) above the solar surface. Again, blue refers to run A, red to run B, and green to run C. As can be seen, the lateral expansion of the front shows very similar evolution for all three runs. The time shift signifies that the front reaches a higher altitude sooner when the magnitude of the acceleration is increased. Interestingly, the time shift at the lowest level is very small, indicating that the primary wave speed shows very little variability as a function of CME acceleration. (This is visible in Figure 4 as well.) The high initial speed for all cases is mainly due to projection effects, as the front first intersects these horizontal levels tangentially. The lateral displacement of the wave front at the lowest height is also affected by the high magnetosonic speed near the flux rope and photospheric sources. The velocity of the front then slowly decelerates in accordance with the decline of the magnetosonic speed away from the simulation center along the x-axis close to the bottom (see Figure 1) and as a result of the diminishing projection effects. Note also that the wave speed at the lowest level is monotonically decreasing as a function of displacement, whereas the leading edge of the primary wave in the emission measure shows acceleration, indicating that the latter is an effect of a wave front bending toward the solar surface with increasing distance.

To eliminate the projection effects, we have also considered the lateral expansion velocity of the wave, defined as the horizontal velocity component of the wave measured at the outermost point (in x) of the wave at any instance. At this point, the wave front is vertical, so the velocity corresponds to the shock velocity at this point. This is plotted in Figure 5 as well. After an initial phase of deceleration, the shock speed at the flank picks up owing to the motion of the vertical part of the wave front to a region with higher Alfvén speed.

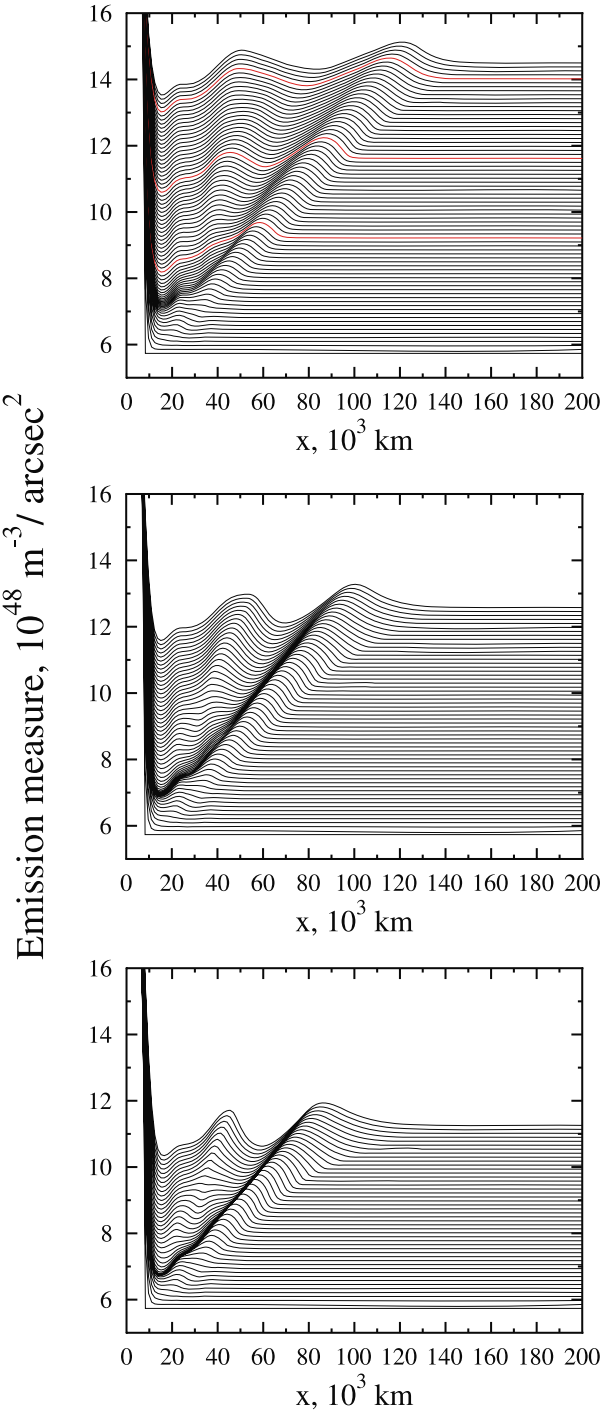

Figure 4 Evolution of the emission measure for the three simulation runs (run A on top, run B in the middle, and run C on the bottom). The scales of the axis are the same for the three plots, and the time interval between the curves is 11 s. The times $t = 330$, 550, and 770 s corresponding to the times of the snapshots in Figure 2 have been indicated by red lines.

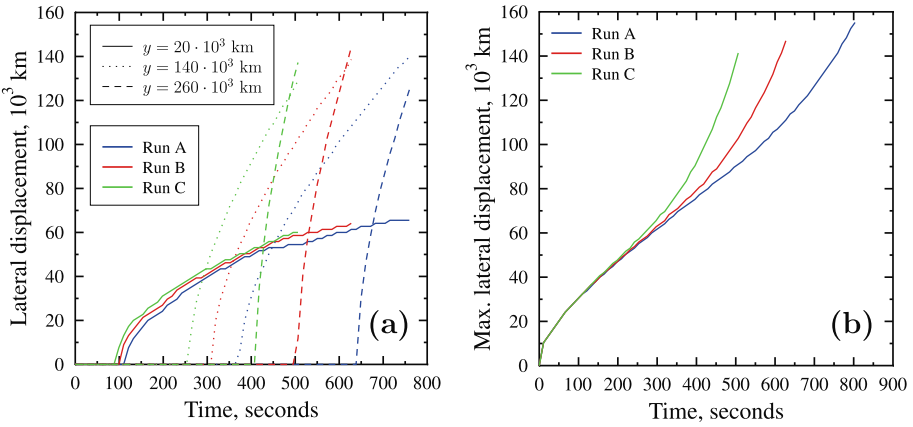

Figure 5 (a) The distance along the x-axis measured from the center of the simulation area to the shock for three different heights for the three simulation runs, and (b) the maximum distance along the x-axis to the front (at any y-level) as a function of time. In both panels, blue corresponds to run A, red to run B, and green to run C.

All runs have very similar evolution of the lateral distance initially, but the final phase of increasing lateral speed starts earlier for flux ropes with higher acceleration.

4. Discussion

We have performed MHD simulations of the CME lift-off employing a simple model of a detached flux rope accelerated through the low corona by an artificial external force. In the following, we will discuss the model results in terms of observations related to CME lift-off.

4.1. Wave Propagation

The model shows several large-amplitude wavelike perturbations that can be linked with waves observed during the CME lift-off.

The flux rope motion launches a coronal shock wave, which propagates in all directions from the driver. It nevertheless remains strongest near the leading edge of the shock, which emphasizes the role of the driver. Although there is no conclusive compression-ratio threshold for the ability of the shock to produce a radio burst, some diagnostics of this are provided by the band-splitting observed during type II bursts: For example, Vršnak *et al.* (2001) studied a number of events and found that the compression ratio deduced from the band-splitting fell between the values of 1.2 and 3.3. In our simulations the compression ratio at the nose of the shock generally exceeds 3 within a couple of minutes after the start of the flux-rope acceleration, so the wave near the leading edge should be strong enough to produce a metric type II radio burst.

The speed of the shock at the leading edge far exceeds the speed of the driver (*i.e.*, once it is formed, the shock can adjust to the local conditions so that it can continue propagating through the corona even if the driver speed falls below the local magnetosonic speed). However, as the driver lags behind the shock and its speed falls clearly below the magnetosonic speed measured at the shock front, the shock starts to lose strength again. Unfortunately, with our 2-D model with Cartesian geometry, it is impossible to follow the shock to the

outer corona to see whether the shock, and the related metric type II burst, would die out before the region of the coronal Alfvén speed maximum at a few solar radii.

Although the compression ratio at the shock is limited below 4 by shock physics, the gas behind the shock front is still further compressed to even higher densities. The density between the shock and the flux rope shows a maximum in between these two levels. There is a local minimum of the density just ahead of the flux rope. This density structure results from a combined effect of the accelerating driver and the ambient Alfvén speed profile.

The flanks of the shock close to the solar surface are rather weak and represent a large-amplitude magnetosonic wave rather than a shock wave, especially during the early phases of the eruption. The emission measure reveals an increase propagating away from the eruption site at a speed in rough correspondence with the local magnetosonic speed. This wave, thus, resembles an EIT wave observed after CME lift-off. During later phases of propagation, especially for rapidly accelerating flux ropes, the wave strengthens and its speed increases above the magnetosonic speed. This is probably because of the refraction of the coronal shock toward the solar surface, which occurs because the Alfvén speed away from the flux rope increases as a function of height. With our driver showing very slow lateral expansion, it is not possible to reproduce typical signatures of chromospheric Moreton waves, which are clearly faster than the magnetosonic speed and strongest close to the flare site. Thus, our results indicate that the presence of a chromospheric Moreton wave may require a lift-off of a much more overpressured flux rope or a thermal explosion-kind of energy release.

Behind the "EIT wave" front, there is a clear depletion of emission measure, which may be related to coronal dimmings also observed after the lift-off of CMEs. In the case of high flux-rope acceleration we also see a secondary wave front propagating through the dimming behind the primary front. The second wave front is launched by the collision of the flow behind the flux rope with the flux rope itself. In our model, the flow is mainly driven by the pressure gradient formed by the evacuation of material, but in a model more prone to magnetic reconnection, it could result from a reconnection jet, as well (Chen *et al.*, 2002). This is an observational feature that could be searched for in EUV images and compared with the CME speed observed from the first couple of images. (This speed gives a measure of the CME acceleration below the field of view of the coronagraph.)

The temperature plot (Figure 2) reveals an arc of extremely hot plasma (downstream of the shock front), which could easily be interpreted as a hot erupting coronal loop. However, the feature is not a loop but a wave. Thus, one must be careful when interpreting propagating looplike features in coronal soft X-ray images. Some of them might actually be shock waves driven by erupting filaments.

4.2. Particle Acceleration

The eruption complex offers many sites favorable for particle acceleration. First, the current sheet forming behind the flux rope will certainly produce a flare and host DC electric fields capable of electron acceleration to high energies. The plasmas in the wave of the erupting flux rope and in the sheath region between the shock and the piston are almost certainly very turbulent, making them ideal for stochastic particle acceleration. Furthermore, the global shock front forming around the erupting flux rope becomes relatively strong (exceeding the compression ratio of 2 at the nose) within 2 – 6 minutes from the start of the eruption for the studied cases, the delay being anticorrelated with the acceleration of the flux rope. The shock wave in our geometry has a quasi-perpendicular region at the nose and at the flanks, and the field lines of the ambient corona are typically intercepted by the shock wave at four

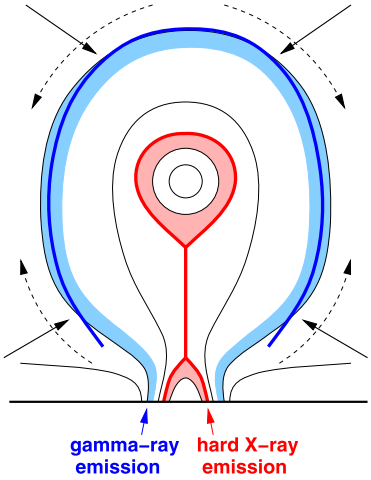

Figure 6 The geometry of the magnetic field and the shock front. The front intersects the field lines at four points, indicated by solid arrows. The points move from top to bottom and from bottom to top along the front, as indicated by dashed arrows. Ions accelerated at the shock precipitate outside the region magnetically connected to the current sheet, which is a source of accelerated electrons.

points (see Figure 6). Quasi-perpendicular parts of the shock can accelerate particles more rapidly than quasi-parallel parts.

The region of the field line left upstream of the shock is in the region of the laterally expanding part of the front (with the shock normal in the horizontal direction). As a given field line becomes completely overtaken by the shock, the shock normal angle increases from a value in the oblique regime to 90 degrees. Particles may in this case be trapped close to the shock and be accelerated to high energies via multiple interactions with the shock front even without strong magnetic scattering in the upstream plasma (Sandroos and Vainio, 2006). In this acceleration process, particles gain speed predominantly parallel to the magnetic field (Sandroos and Vainio, 2006) and, therefore, they can more easily precipitate to the solar surface in spite of the strong magnetic mirroring. Note that the field lines traversing the shock are connected to the region at the solar surface somewhat outward from those field lines connected to the current sheet below the flux rope. However, electron acceleration at reconnecting current sheets is generally acknowledged as being one of the most plausible mechanisms to account for the hard X-ray flares. As the parallel electric fields cannot be adequately modeled by an ideal MHD simulation, a detailed analysis of electron acceleration below the erupting filament is beyond the scope of this paper. Nonetheless, it is interesting to note that if ions are accelerated at the shock and electrons predominantly at the current sheet, our magnetic field geometry would be consistent with gamma rays being emitted somewhat outside of the hard X-ray sources, as observed by RHESSI (Lin *et al.*, 2003). We intend to revisit this issue in future studies using test-particle simulations.

5. Conclusion

In conclusion, our simplified MHD model of perturbations caused by an erupting flux rope reproduces qualitatively surprisingly many dynamic features observed during the CME lift-off. The key features of the model include an accelerating flux rope acting as a piston and pushing the ambient plasma in motion and a coronal magnetic field and density structure producing an ambient magnetosonic speed that increases with height. Together they can reproduce, for example, coronal shocks that may drive metric type II radio bursts, EIT waves, coronal dimmings, and sites of particle acceleration consistent with electromagnetic observations of flares and CMEs at different wavelengths.

Acknowledgements J.P. and R.V. thank the participants of the Working Group 4 of the CESRA Meeting in Ioannina, June 2007, for fruitful discussions concerning the MHD modeling of CME-related waves and mass motions. Financial support from the Vilho, Yrjö, and Kalle Väisälä foundation is acknowledged. A part of this work was financed by the Deutsche Forschungsgemeinschaft (DFG) through the project KL 650/6. Finally, the authors thank the referee for the useful comments.

References

Cane, H.V., Mewaldt, R.A., Cohen, C.M.S., von Rosenvinge, T.T.: 2006, *J. Geophys. Res.* **111**, A06S90. doi:10.1029/2005JA011071.

Chen, P.F., Wu, S.T., Shibata, K., Fang, C.: 2002, *Astrophys. J.* **572**, L99.

Kissmann, R.: 2007, *Numerical investigation of the turbulent ISM*. Ph.D. thesis, Ruhr-Universität Bochum. Available at http://deposit.ddb.de/cgi-bin/dokserv?idn=98361265x.

Kocharov, L., Lytova, M., Vainio, R., Laitinen, T., Torsti, J.: 2005, *Astrophys. J.* **620**, 1052.

Lin, R.P., Krucker, S., Hurford, G.J., Smith, D.M., Hudson, H.S., Holman, G.D., *et al.*: 2003, *Astrophys. J.* **595**, L69.

Moreton, G.E., Ramsey, H.E.: 1960, *Publ. Astron. Soc. Pac.* **72**, 375.

Reames, D.V.: 1999, *Space Sci. Rev.* **90**, 413.

Sandroos, A., Vainio, R.: 2006, *Astron. Astrophys.* **455**, 455.

Sandroos, A., Vainio, R.: 2007, *Astrophys. J.* **662**, L127.

Thompson, B.J., Gurman, J.B., Neupert, W.M., Newmark, J.S., Delaboudinière, J.-P., St. Cyr, O.C., *et al.*: 1999, *Astrophys. J.* **517**, L151.

Tylka, A.J., Lee, M.A.: 2006, *Astrophys. J.* **646**, 1319.

Tylka, A.J., Cohen, C.M.S., Dietrich, W.F., Lee, M.A., Maclennan, C.G., Mewaldt, R.A., Ng, C.K., Reames, D.V.: 2005, *Astrophys. J.* **625**, 474.

Vainio, R., Khan, J.: 2004, *Astrophys. J.* **600**, 451.

Vainio, R., Kocharov, L., Laitinen, T.: 2000, *Astrophys. J.* **528**, 1015.

Vršnak, B., Aurass, H., Magdalenić, J., Gopalswamy, N.: 2001, *Astron. Astrophys.* **377**, 321.

Wild, J.P., McCready, L.L.: 1950, *Aust. J. Sci. Res.* **3**, 387.

Ziegler, U.: 2004, *J. Comput. Phys.* **196**, 393.